



OPEN

Structure–function characterization of an aldo–keto reductase involved in detoxification of the mycotoxin, deoxynivalenol

Nadine Abraham^{1,2}, Kurt L. Schroeter¹, Yan Zhu², Jonathan Chan^{1,2}, Natasha Evans^{1,2}, Matthew S. Kimber¹, Jason Carere², Ting Zhou² & Stephen Y. K. Seah¹✉

Deoxynivalenol (DON) is a mycotoxin, produced by filamentous fungi such as *Fusarium graminearum*, that causes significant yield losses of cereal grain crops worldwide. One of the most promising methods to detoxify this mycotoxin involves its enzymatic epimerization to 3-*epi*-DON. DepB plays a critical role in this process by reducing 3-keto-DON, an intermediate in the epimerization process, to 3-*epi*-DON. DepB_{Rleg} from *Rhizobium leguminosarum* is a member of the new aldo–keto reductase family, AKR18, and it has the unusual ability to utilize both NADH and NADPH as coenzymes, albeit with a 40-fold higher catalytic efficiency with NADPH compared to NADH. Structural analysis of DepB_{Rleg} revealed the putative roles of Lys-217, Arg-290, and Gln-294 in NADPH specificity. Replacement of these residues by site-specific mutagenesis to negatively charged amino acids compromised NADPH binding with minimal effects on NADH binding. The substrate-binding site of DepB_{Rleg} is larger than its closest structural homolog, AKR6A2, likely contributing to its ability to utilize a wide range of aldehydes and ketones, including the mycotoxin, patulin, as substrates. The structure of DepB_{Rleg} also suggests that 3-keto-DON can adopt two binding modes to facilitate 4-*pro-R* hydride transfer to either the *re*- or *si*-face of the C3 ketone providing a possible explanation for the enzyme's ability to convert 3-keto-DON to 3-*epi*-DON and DON in diastereomeric ratios of 67.2% and 32.8% respectively.

Mycotoxins are toxic secondary metabolites produced by filamentous fungi that pose a serious health safety risk for humans and livestock¹. Deoxynivalenol (DON), belongs to a class of *Fusarium* mycotoxins termed trichothecenes which share a tetracyclic sesquiterpene carbon skeleton². Commercial cereal grain crops infected by toxigenic *Fusarium* species show diminished quality, and yield, and often contain high levels of DON. The FDA estimates crop losses due to mycotoxins in the US alone, to be around \$932 million annually, fueling the need for more effective management strategies³.

DON is a potent protein synthesis inhibitor that blocks the A-site of ribosomes, hindering aminoacyl tRNA binding and preventing peptidyl transferase activity⁴. The ribosome interaction is mediated through hydrogen bond contacts from the C12, 13 epoxide ring, C3 hydroxyl, and van der Waal contacts between the C9, C10 double bond⁵. Together, these substituent groups contribute to DON's overall toxicity. Certain bacteria, such as *Devosia mutans* 17-2-E-8 enzymatically detoxify DON by stereochemically inverting the C3 OH from the (S)-configuration to the (R)-configuration producing the diastereomer, 3-*epi*-DON⁶. This impairs binding to the ribosome and overall, reduces its toxicity; as evidenced by MTT bioassays, 3-*epi*-DON possesses an IC₅₀ 357 times higher than DON⁷. This process, termed 'DON epimerization' (Dep) occurs in two stages⁸. First DepA, a PQQ-dependent alcohol dehydrogenase oxidizes the C3 OH group of DON to form 3-keto-DON⁹. A second enzyme, DepB, then reduces 3-keto-DON at the *re*-face of this stereogenic center to produce 3-*epi*-DON^{8,10} (Fig. 1). The intermediate, 3-keto-DON is only moderately less toxic than DON with an IC₅₀ 3-times higher than DON⁷. Therefore, the critical step of DON detoxification is catalyzed by DepB.

DepB belongs to the aldo–keto reductase (AKR) family of enzymes. These ubiquitous oxidoreductases occur in all domains of life, and they catalyze the reduction of diverse carbonyl substrates. They play vital roles in steroid hormone metabolism¹¹, oxidative stress responses^{12,13}, xenobiotic detoxification¹⁴, and are implicated in certain

¹Department of Molecular and Cellular Biology, University of Guelph, Guelph, Canada. ²Guelph Research and Development Centre, Agriculture and Agri-Food Canada, Guelph, ON, Canada. ✉email: sseah@uoguelph.ca

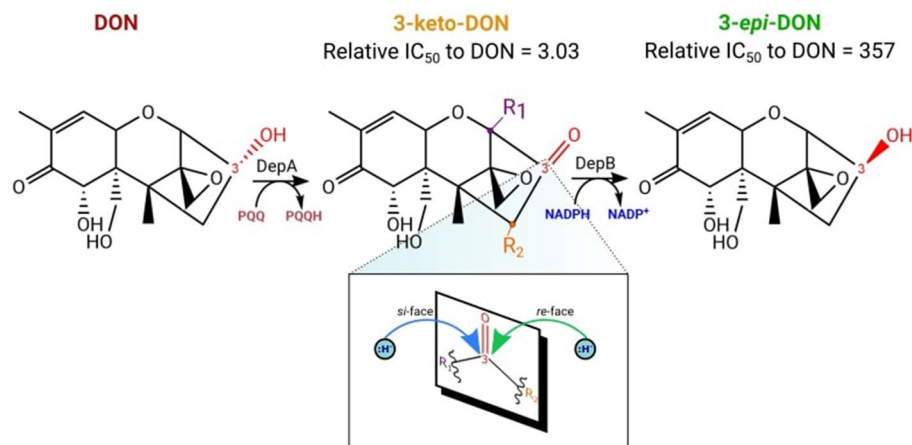


Figure 1. The Dep pathway. The C3 OH group of DON (shown in red) is stereochemically inverted to produce the diastereomer, 3-*epi*-DON. In the expanded image of this stereogenic center, R₁ and R₂ represent the priority groups attached to the *sp*² hybridized C3. Hydride attack on the *re*-face at the prochiral C3 center generates 3-*epi*-DON.

cancers¹⁵ and metabolic disorders such as diabetes^{16,17}. Most AKRs are monomeric proteins with molecular weights ranging from 34 to 37 kDa and predominantly utilize NADP(H) as their coenzyme.

Here we present the crystal structure of DepB from *Rhizobium leguminosarum* (herein designated as DepB_{Rleg}). We determined that DepB_{Rleg} belongs to a recently discovered family of AKRs and although it can use either NADH or NADPH as a coenzyme, the structural basis for its strong preference for NADPH is unknown. Although the stereochemistry of hydride transfer is well established for AKRs, the stereoselectivity of the reduction process, which is key to detoxification, is a less explored avenue. We, therefore, probed the determinants of DepB_{Rleg}'s unusual coenzyme specificity and propose features of the substrate-binding site which dictate the stereochemical outcome of 3-keto-DON reduction through molecular modeling studies. In addition to its role in the Dep pathway, DepB_{Rleg} is also active towards a wide range of aldehyde and ketone substrates including the mycotoxin patulin, making it a versatile biocatalyst for the decontamination of various xenobiotics.

Results

SSN cluster analysis of DepB_{Rleg} with AKRs. AKRs are traditionally classified into families based on sequence identity and phylogenetic analysis. The nomenclature system consists of the root symbol AKR, followed by an arabic numeral designating the family and an alphabet representing the subfamily¹⁸. The number of AKRs in the protein database continues to expand and to date 18 families have been identified. Protein sequences in each family share at least 40% sequence identity while sub-families share 60% sequence identity¹⁹. We used a protein sequence similarity network (SSN)²⁰ as an alternate, less computationally demanding method to determine sequence relationships of DepB_{Rleg} with other AKR family members. For ease of computation, sequences were iteratively clustered to produce a 40% representative node network and filtered based on sequence length. The total number of sequences following the reduction of the initial dataset is 878. In this network, nodes represent protein sequences sharing 40% or more sequence identity and edges represent the pairwise alignments between protein sequences. Edges were drawn between nodes if they exceeded the prescribed stringency threshold or BLAST E-value of e^{-57} .

Previous phylogenetic analysis showed that AKRs can be divided into two large groups with AKR1-AKR5 forming one branch of the phylogenetic tree and the other AKRs forming a separate branch²¹. This is generally reflected in the SSN topology where AKR1 to AKR5 family members cluster together (Fig. 2A). At this stringency threshold, there was good delineation of AKR7-11 and AKR 13-15 into distinct, isofunctional clusters. DepB_{Rleg} and its homologs from *D. mutans* 17-2-E-8¹⁰ and AKR18A1 from *Sphingomonas* S3-4²² clustered with AKR6, AKR12, and AKR14 families. At higher stringency thresholds (e^{-67}), DepB_{Rleg} and its closest homologs resolve into a single isofunctional cluster (Fig. 2B). Curiously, in vitro assays previously revealed that AKR18A1 reduces 3-keto-DON to DON rather than 3-*epi*-DON in the presence of NADH²². The enzyme also reduces the C7 ketone group of the estrogenic mycotoxin, zearalenone (ZEN) to produce α -zearalenol (α -ZOL) and β -zearalenol (β -ZOL). Aside from this, AKR18A1's substrate specificity towards other endogenous aldehydes and ketones has not been examined, nor has its crystal structure been solved.

Besides AKR18A1, the next closest homologs of DepB_{Rleg} identified from this SSN analysis were AKR12 family members based on the first stringency cut-off threshold (e^{-57}). As per AKR classification rules, DepB_{Rleg} is not an AKR12 family member as it shares less than 40% sequence identity with enzymes from this family. In addition, these AKR12 members are involved in the biosynthetic pathways of polyketide macrolide antibiotics such as tylosin, erythromycin, and avermectin²³⁻²⁵. A genome neighborhood diagram (GND) of DepB_{Rleg} revealed the presence of a putative monoamine oxidase (MAO) upstream of the DepB_{Rleg} gene along with several putative

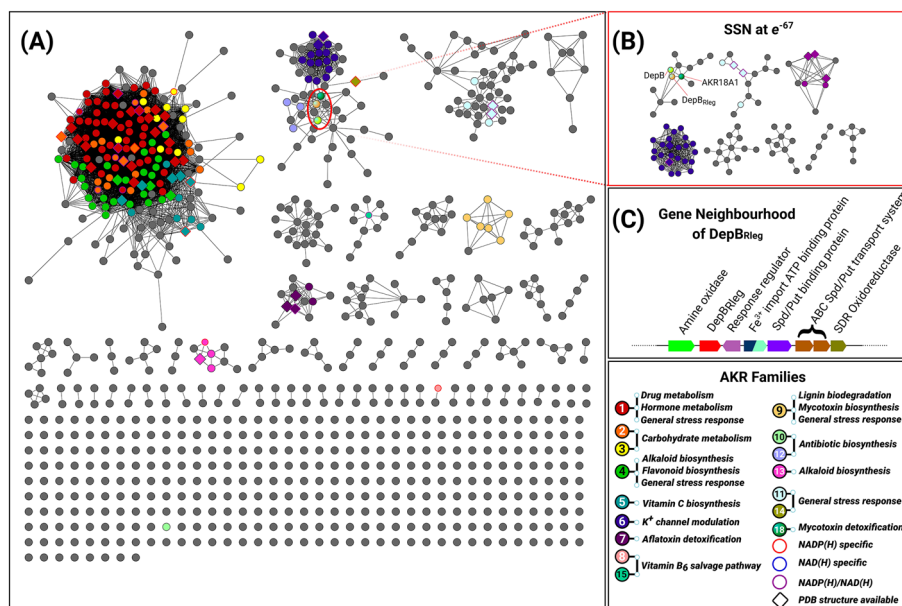


Figure 2. A 40% representative sequence similarity network (SSN) at a threshold of e^{-57} . **(A)** Nodes within each cluster contain a representative protein sequence of a collection of sequences that share 40% or more sequence identity. Clusters have been annotated and color-coded based on curated protein sequences from the AKR Database²¹. Grey nodes represent AKRs that have no functional annotation. Metabolic pathways associated with the function of AKR enzymes have been color-coded to cross-reference with each cluster and numerically labeled to designate each AKR family number. The nodes of AKRs possessing biochemical data on coenzyme specificity and crystal structures have also been accordingly labeled as outlined in the legend. **(B)** SSN generated at a threshold of e^{-67} depicting complete segregation of the AKR18 family from AKR6, AKR12 and AKR14 members. **(C)** Genome Neighborhood Diagram of *DepB_{Rleg}*. The GND was generated using the EFI-GNT server which depicts the coding sequence region of *depB_{Rleg}* along with putative functions of upstream and downstream genes.

spermidine/putrescine transporter genes downstream of *DepB_{Rleg}* (Fig. 2C). The neighboring genes reported for the *depB* homolog in *D. mutans* 17-2-E-8 differ from *depB_{Rleg}* but are also not polyketide synthesis genes¹⁰.

Substrate specificity profile of *DepB_{Rleg}*. Recombinant N-terminal His-tagged *DepB_{Rleg}* was purified to homogeneity by Ni-NTA chromatography. A band corresponding to a molecular weight of approximately 39 kDa was observed on a 10% SDS-PAGE gel (See Supplementary Fig. S1). The substrate specificity of the purified enzyme towards 3-keto-DON, aliphatic and aromatic carbonyl compounds, as well as nicotinamide cofactors were assessed by steady-state kinetics (Table 1). *DepB_{Rleg}* possesses the highest specificity constant (k_{cat}/K_m) with the diketone 9,10-phenanthrenequinone (9,10-PQ) on the order of 27 times higher relative to 3-keto-DON and 35 times higher relative to the smaller diketone, isatin. *DepB_{Rleg}* is also active towards endogenous toxic aldehydes derived from oxidative stress responses such as lipid peroxidation^{26,27}. These aldehydes include acrolein, methylglyoxal, 4-oxo-2-nonenal, 4-hydroxy-2-nonenal, hexanal, and butanal. Among the aldehydes, *DepB_{Rleg}* displayed high specificity constants for the smaller unsaturated aldehydes such as acrolein and methylglyoxal, although the K_m for methylglyoxal was too high to be determined reliably. Among the $\alpha\beta$ unsaturated aliphatic aldehydes, 60-fold higher specificity constant was observed for 4-oxo-2-nonenal compared to 4-hydroxy-2-nonenal. The apparent K_m for NADPH is about 100-fold lower than NADH ($15.2 \pm 1.41 \mu\text{M}$ vs. $1560 \pm 399 \mu\text{M}$) when evaluated using DL-glyceraldehyde as a substrate at a fixed concentration of 10 mM, while the apparent k_{cat} with NADPH was only 13-fold higher than with NADH ($0.337 \pm 0.00757 \text{ s}^{-1}$ vs. $0.0242 \pm 0.00344 \text{ s}^{-1}$). *DepB_{Rleg}* was also determined to reduce the mycotoxin patulin but not citrinin. Both these mycotoxins are produced by *Penicillium expansum* which is the causative agent of blue mold rot in apples²⁸. LC-MS/MS analysis indicated that patulin was indeed transformed to E-ascladiol, a by-product previously reported to be significantly less cytotoxic compared to patulin^{29,30}. The mechanistic basis for this transformation has been proposed to involve the spontaneous opening of the hemiacetal ring of patulin followed by the reduction of the aldehyde to the alcohol³¹ (See Fig. S2 for LC-MS/MS results).

Crystallization and structure determination of *DepB_{Rleg}*. *DepB_{Rleg}* was successfully crystallized, and its structure was solved by molecular replacement using an AKR from *Polaromonas* sp. JS666 as a search model (PDB ID: 4XK2). Structural and refinement statistics are summarized in Table 2.

Four protomers of *DepB_{Rleg}* are present in the asymmetric unit designated as chains A, B, C, and D. Overall, the three-dimensional structure of each protomer adopts the classic triose-phosphate isomerase (TIM) barrel fold (α/β)₈, except that the presence of Pro-204 in the region that would otherwise form strand $\beta 7$ disrupts the

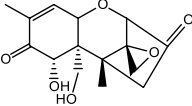
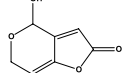
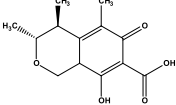
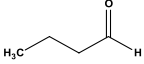
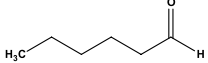
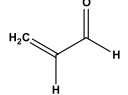
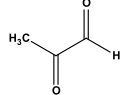
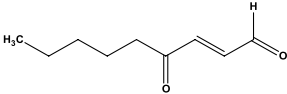
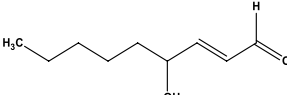
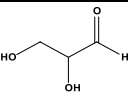
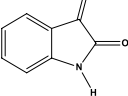
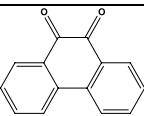
Substrate	Structure	$K_{m,app}$ (μM)	$k_{cat,app}$ (s^{-1})	k_{cat}/K_m ($\text{M}^{-1} \text{s}^{-1}$)
Mycotoxins				
3-keto-DON		645 ± 60.3	3.01 ± 0.104	4670 ± 465
Patulin		678 ± 85.5	0.0100 ± 0.000590	14.7 ± 2.05
Citrinin		n.a.	n.a.	n.a.
Aliphatic aldehydes				
Butanal		617 ± 33.5	0.410 ± 0.00922	665 ± 39.1
Hexanal		1230 ± 231	0.303 ± 0.0269	246 ± 51.1
Unsaturated aldehydes				
Acrolein		83.3 ± 6.69	0.0677 ± 0.00159	813 ± 68
α-keto aldehyde				
Methylglyoxal		n.d.	n.d.	2110*
$\alpha\beta$-unsaturated aliphatic aldehydes				
4-oxo-2-nonenal		1020 ± 136	7.90 ± 0.678	7750 ± 1230
4-hydroxy-nonenal		n.d.	n.d.	130*
Aldotriose				
DL-Glyceraldehyde		3890 ± 516	0.782 ± 0.0803	201 ± 33.7
Di-ketones				
Isatin		1780 ± 410	6.43 ± 0.920	3610 ± 979
9,10-PQ		68.3 ± 14.3	8.76 ± 0.84	128000 ± 29500

Table 1. Substrate specificity profile of DepB_{Rleg}. Apparent kinetic parameters for reduction of model aldehydes and ketones by recombinant DepB_{Rleg} in the presence of 1 mM NADPH. (n.d. = not determined, n.a. = no activity, *estimated from the gradient of the v vs. [S] slope).

hydrogen bonding pattern leaving this region as an extended loop. Two auxiliary helices designated as H1 and H2 are found at the periphery of the barrel, while the N-terminal end of the barrel is capped by an N-terminal β -hairpin loop. The TIM barrel scaffold contains $\beta\alpha$ loops that connect β -strands to α -helices and the $\alpha\beta$ loops that connect α -helices to β -strands. $\beta\alpha$ loops are longer than $\alpha\beta$ loops and impart structural and hence functional diversity to TIM barrel proteins such as AKRs³². The $\beta3\alpha3$ loop (designated as Loop A) and the C-terminal loop (designated as Loop C) are proposed to govern substrate binding in AKRs while the primary role of the longer $\beta7\text{H}1$ loop (designated as Loop B) is for coenzyme binding³³ (Fig. 3A). Due to a lack of clear electron density, the following residues within loop B could not be modeled: Chain A (214–241), Chain B (217–244), Chain C (219–245), and Chain D (218–245).

Data collection	
Space group	<i>P4</i> 2 ₁ 2
Cell dimensions	
<i>a</i> , <i>b</i> , <i>c</i> (Å)	159.45, 159.45, 163.90
α , β , γ (°)	90.00, 90.00, 90.00
Resolution (Å)	46.45–2.5 (2.589–2.5)*
Total reflections	1,202,979 (120,250)
No. of unique reflections	73,419 (7223)
<i>R</i> _{merge}	0.2617 (2.503)
<i>I</i> / σ <i>I</i>	11.52 (1.30)
Completeness (%)	99.81 (99.81)
Redundancy	16.4 (16.6)
Refinement	
Resolution (Å)	
No. reflections	73,312 (7214)
<i>R</i> _{work} / <i>R</i> _{free}	0.1847/0.2341
No. atoms	2038
Protein	1275
Ligand/ion	188
Water	575
Wilson <i>B</i> -factors	47.35
<i>B</i> -factors	
Protein	61.26
Ligand/ion	89.53
Water	53.87
R.m.s deviations	
Bond lengths (Å)	0.002
Bond angles (°)	0.45
Ramachandran statistics	
Favored (%)	95.31
Allowed (%)	3.97
Outliers (%)	0.71

Table 2. X-ray diffraction data and refinement statistics. *Highest resolution shell is shown in parentheses.

A pair of protomers (A and C, B and D) associate together forming a dimer with an average interface area of 2362.9 Å², stabilized by 24 hydrogen bonds and 13 salt bridges. Dimerization involves 3D domain swapping with the exchange of the α -helix of loop C which interacts with loop A on the associating protomer. These dimers interact around the crystallographic four-fold symmetry axis to form a D₄ symmetric octamer (Fig. 3B), with key interactions mediated by the N-terminal β -hairpin, α 3, α 4, and the β 4 α 4 loop. PISA³⁴ estimates that these interactions bury 748.6 Å² and result in a solvation-free energy gain of -809.8 kcal/mol. The absolute molecular weight of DepB_{Rleg} was determined experimentally by SEC-MALS to be 325.6 ± 12.1 kDa which is consistent with the 317.5 kDa predicted for a DepB_{Rleg} octamer. (See Supplementary Fig. S3).

The closest structural homologs of DepB_{Rleg} are the functionally uncharacterized AKRs from the structural genomics initiative, *Polaromonas* sp. AKR (PDB ID: 4XK2, 44% sequence identity, 1.6 Å RMSD), an *Escherichia coli* AKR, Tas (PDB ID: 1LQA, 35% sequence identity, 2.0 Å RMSD), that has broad substrate specificity³⁵, the beta subunit of the voltage-gated potassium channel from *Rattus norvegicus* (AKR6A2; PDB ID: 3EAU, 32% sequence identity, 2.1 Å RMSD), *E. coli* AKR14A1 (PDB ID: 4AUB, 35% sequence identity, 2.4 Å RMSD) that is specific towards methylglyoxal and diketones such as isatin³⁶ and mithramycin side chain reductase from *Streptomyces argillaceus* (PDB ID: 6OW0, 33% sequence identity, 2.3 Å RMSD). Mithramycin side chain reductase is a ketoreductase that reduces the 4' ketone side chain of mithramycin DK, an intermediate in the biosynthesis of the tricyclic antitumor polyketide, mithramycin³⁷.

Diversity in certain loop regions was observed among these structural homologs. Differences in the conformation of loop B and the auxiliary helices, H1 and H2 could be due to conformational changes upon binding of NADP(H) and/or substrates. Loop B in the apo-structures of DepB_{Rleg} and *Polaromonas* sp. AKR is disordered, but clear electron densities for this region were observed for the NADP⁺ binary complexes of the other structural homologs. This is in agreement with the finding that loop B becomes ordered upon coenzyme binding³⁸. In addition to these conformational differences, variations in loop length are also evident, particularly for the *E. coli* Tas protein which possesses a long α 4 β 4 loop (24 residues) compared with DepB_{Rleg} (8 residues). The length and structure of DepB_{Rleg} loop C (26 residues) also differed with AKR6A2 (6 residues), Tas (5 residues), AKR14A1 (10 residues), and mithramycin side chain reductase (6 residues). In the hydroxysteroid reductase subfamily of

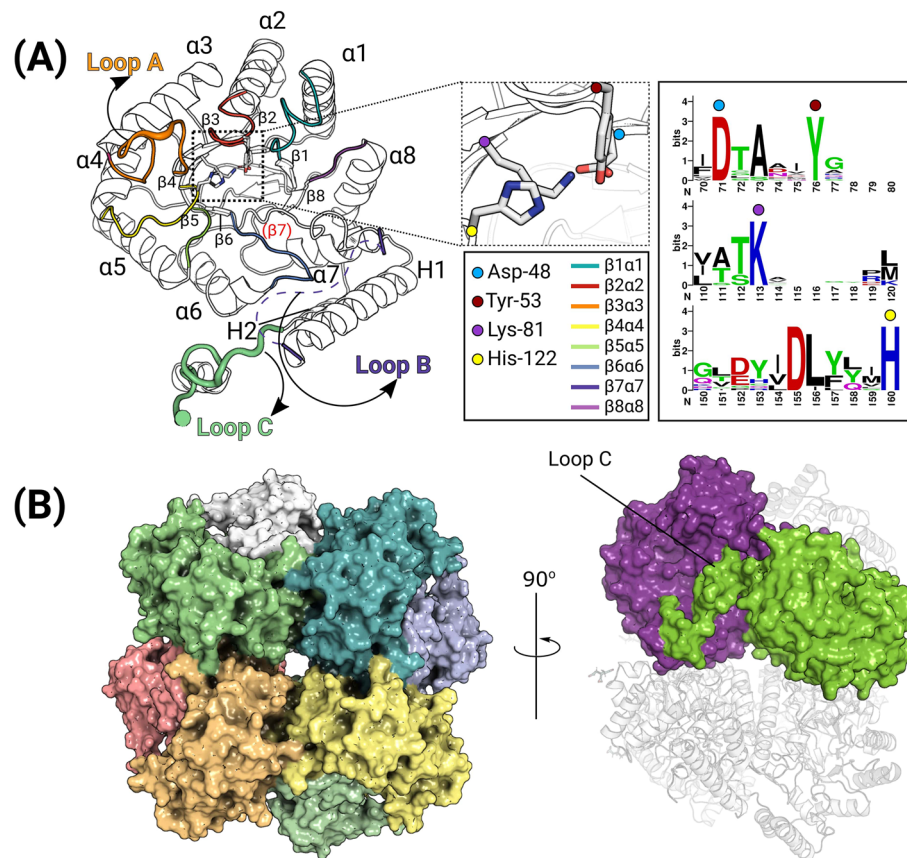


Figure 3. Crystal structure of DepB_{Rleg} protomer and octameric assembly. (A) Cartoon representation of the protomer with a view looking down the top of the TIM barrel rendered in black and white with the β7 annotated in red. Loop A (orange) caps the top of the substrate-binding cleft, loop B (dashes) could not be modeled but its position has been highlighted in this figure, and finally, loop C (green) which extends into the active site of the opposing protomer in the dimer. A sequence logo highlighting the conservation of the catalytic residues has also been provided. (B) Surface and cartoon rendition of the DepB_{Rleg} octamer. This assembly was predicted using the PISA server. View rotated at a 90° angle depicting 3D domain swapping of loop C at the dimer interface.

AKRs truncation of this loop led to reduced specific activity towards steroid substrates, therefore the diversity in loop lengths among these AKRs likely contributes to corresponding differences in substrate specificity³⁹.

Coenzyme binding site. DepB_{Rleg} reduced 3-keto-DON using NADH and NADPH as coenzymes, although the catalytic efficiency with NADH was 40-times lower than with NADPH. The dissociation constant (K_d) for NADH, as determined by tryptophan fluorescence quenching experiments, was about sixfold higher than NADPH. In contrast, most AKRs are NADPH specific with NADPH dissociation constants on average, 1000-fold lower than NADH⁴⁰. DepB_{Rleg}, therefore, shares the rare dual coenzyme specificity with a small number of enzymes from different AKR families, including the hydroxysteroid dehydrogenases (AKR1C)^{41,42}, xylose reductases (AKR2B)^{43–45}, beta subunit of voltage-gated potassium ion channels (AKR6A)⁴⁶, aflatoxin reductases (AKR7A)⁴⁷, and pyridoxal dehydrogenases (AKR15A)⁴⁸. The structural basis for NADH specificity was studied for *Candida tenuis* xylose reductase (AKR2B5), revealing a key Glu-227 residue on loop B which forms bidentate hydrogen bonds with the 2' and 3' hydroxyl groups of the adenosine moiety of NAD⁺⁴⁴. In DepB_{Rleg}, this residue is also conserved and corresponds to Glu-222. In the NADP⁺ bound complex of AKR2B5, the 2' monophosphate of NADP⁺ interacts with a positively charged Arg-280, the peptide backbone of Asn-276, and Ser-275. These residues are not strictly conserved in DepB_{Rleg} and are instead replaced with Gln-294, Arg-290, and Ala-288, underscoring the general variability in NADP⁺ interactions among the AKRs.

Although NADP⁺ was present at 400 μM during the crystallization of DepB_{Rleg}, there was no electron density corresponding to this coenzyme. The putative coenzyme binding pocket was suitably defined and superimposed well with coenzyme binding sites of AKR binary complexes. AKRs bind NADPH in an extended *anti*-conformation to achieve the stereospecificity of hydride transfer³³. An aromatic residue typically forms π-stacking interactions with the nicotinamide ring while the carboxamide moiety is oriented by highly conserved glutamine, serine, and asparagine residues. In DepB_{Rleg}, these residues correspond to Trp-206, Gln-178, Ser-152, and Asn-153 respectively. In AKR6A2, the closest structural homolog of DepB_{Rleg}, the 2' monophosphate of NADP⁺ interacts with the side chains of Gln-62, Lys-254, Ser-325, and Gln-329, and (Fig. 4A). In DepB_{Rleg}, these residues correspond to Glu-26, Lys-217, Arg-290, and Gln-294 respectively. To examine the conservation of these residues, a

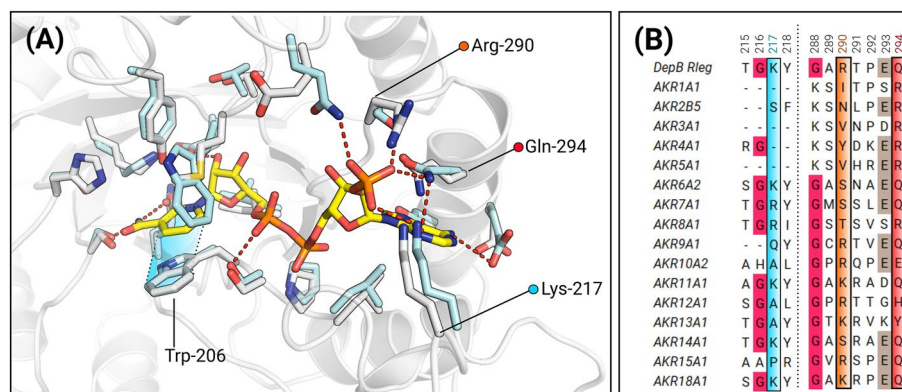


Figure 4. Model of the coenzyme binding site highlighting the conservation of putative coenzyme binding residues. **(A)** NADP⁺ was modeled by superimposing the ternary complex of AKR6A2 with apo-DepB_{Rleg}. White sticks represent the residues from DepB_{Rleg} complex, while cyan sticks are residues corresponding to AKR6A2. Trp-206 has been re-oriented in the apo-DepB_{Rleg} structure to prevent a steric clash with the nicotinamide ring of NADP⁺. π -stacking interactions between the nicotinamide ring and Trp-206 are shaded in blue. In apo-DepB_{Rleg}, Lys-217 points away from the entrance of the coenzyme binding pocket. However, by analogy to Lys-254 in AKR6A2, this residue may interact with at least one of the oxygen atoms of 2' monophosphate. **(B)** MSA depicting conservation of residues near the 2' monophosphate of the modeled NADP⁺ (See Supplementary Table S1 for accession codes).

Enzyme	K_d (μ M)		$K_d^{\text{NADPH}}/K_d^{\text{NADH}}$
	NADPH	NADH	
DepB _{Rleg}	11.4 \pm 0.84	67.3 \pm 2.5	0.17
R290E	123 \pm 6.2	119 \pm 9.8	1.03
R290N	59.5 \pm 4.2	77.7 \pm 3.6	0.76
Q294E	97.9 \pm 13	91.2 \pm 10	1.07
K217E	68.6 \pm 8.7	87.1 \pm 3.4	0.79
K217M	74.1 \pm 4.6	82.9 \pm 3.0	0.89

Table 3. Apparent coenzyme dissociation constants for purified recombinant DepB_{Rleg} and coenzyme variants.

multiple sequence alignment was constructed with AKR family representatives. Lys-217 which is present on loop B is not strictly conserved and is often substituted for a basic residue or a smaller hydrophobic residue. Arg-290 is partially conserved across the AKR families and this position is often frequented by a basic residue or a polar hydrophilic residue. Gln-294 is strictly conserved across AKR6A2, AKR7A1, AKR9A1, AKR11A1, AKR14A1, AKR15A1, and AKR18A1 but for the other families, it is replaced with either a basic or aromatic residue (Fig. 4B). Lastly, Glu-26 was the least conserved and was therefore not selected for further analysis.

All recombinant N-terminal His-tagged DepB_{Rleg} coenzyme variants were purified by Ni-NTA chromatography with expected molecular weights of 39 kDa (See Supplementary Fig. S1). Replacements of Lys-217, Arg-290, and Gln-294 for negatively charged glutamate significantly altered the K_d for NADPH relative to wild type DepB_{Rleg}, with no significant effect on the K_d of NADH. Among these variants, the R290E variant displayed an 11-fold increase, followed closely by Q294E with a ninefold increase and finally K217E with only a sixfold change (Table 3). Substitutions for neutral residues as in the case for R290N displayed a moderate change in the K_d by fivefold, while for K217M, the K_d change relative to the wild type was more pronounced with a nearly sevenfold change. Overall, for all the mutants, there was no appreciable change in K_d for NADH.

Substrate-binding site. The catalytic mechanism of AKRs involves a stereospecific 4-*pro*-R hydride transfer from the nicotinamide ring of the coenzyme to the substrate carbonyl carbon, followed by protonation of the carbonyl oxygen by a tyrosyl residue⁴⁹. This is facilitated by a proton relay with histidine or a lysine-aspartate pair⁴⁰. In DepB_{Rleg}, these catalytic residues are conserved: Asp-48, Tyr-53, Lys-81, and His-122. A water molecule occupies the position equivalent to the carbonyl oxygen group of the substrate and forms hydrogen bonds (2.6–2.9 Å) to the side chains of both His-122 and Tyr-53⁴⁹. DepB_{Rleg}'s substrate-binding pocket is lined with the following residues: Met-21, Asp-48, Val-52, Tyr-53, Lys-81, Arg-83, Phe-84, His-122, Ala-123, Ser-152, Asn-153 and Gln-180. Overall, DepB_{Rleg}'s substrate-binding pocket is slightly larger and more hydrophobic in comparison with the NADP⁺-cortisone bound complex of AKR6A2. The physiological substrate of AKR6A2 is unknown, however, much like DepB_{Rleg} it also displays broad substrate specificity with aldehyde and ketone substrates⁵⁰.

dehydrogenase family of oxidoreductases^{56,57}. In summary, the broad substrate specificity of this AKR, therefore, lends credence to its secondary role in general detoxification processes.

A consensus among most AKRs is their preference for the coenzyme, NADPH over NADH⁴⁹. Investigations of the coenzyme binding affinities of DepB_{Rleg} revealed that it can utilize both NADPH and NADH, albeit with preference for NADPH over NADH. Given that NADPH is more expensive than NADH, the ability of DepB_{Rleg} to utilize NADH as a coenzyme will be beneficial for its use as a biocatalyst to detoxify DON. Based on comparative structural analysis, the residues Lys-217, Arg-290, and Gln-294 are proposed as key contributing elements for DepB_{Rleg}'s preference for NADPH. These structural elements likely contribute to a hydrogen bond network encompassing the 2' monophosphate of NADPH. Precedents for coenzyme specificity are well established for short-chain dehydrogenases (SDRs). In NADP⁺ dependent SDRs, a basic residue in the glycine-rich motif of the Rossmann fold governs NADP⁺ specificity while for NAD⁺ dependent SDRs, typically an aspartate or glutamate is present⁵⁸. Similarly, in DepB_{Rleg}, the basic residues, Arg-290 and Lys-217 contribute the necessary salt-bridge interactions with the 2' monophosphate, while Gln-294 also provides hydrogen bond interactions and provides planar stacking interactions between the amide group of its side chain and the adenosine ring. Not surprisingly, substitutions for negatively charged residues generated electrostatic repulsion with the 2' monophosphate group resulting in an increased NADPH K_d value for R290E, Q294E, and K217E. While the change in K_d for the R290N variant was not as dramatic, we rationalize that replacement of the arginine for a polar, shorter residue like asparagine likely altered the hydrogen bond network coordinating the 2' monophosphate which consequently affected the binding mode of NADPH. K217M and K217E displayed a similar increase in K_d for NADPH, however, the effect was not as pronounced as in the Arg-290 variants. As Lys-217 is present on Loop B, which displays a great deal of sequence variance, it is plausible that a proximal, basic residue may have compensated for the absence of the lysine residue in the K217M and K217E variants.

Reduction of 3-keto-DON by DepB_{Rleg} produced 3-*epi*-DON and DON in diastereomeric ratios of 67.2% and 32.8% respectively. Modeling suggests that the formation of the two diastereomers is due to alternate 3-keto-DON binding modes that enable the *re* or *si*-face to approach the 4-*pro*-R hydrogen of the nicotinamide cofactor. Although DepB_{Rleg} does not show strict diastereoselectivity towards 3-*epi*-DON formation, coupling the enzyme with DepA which has an apparent K_m of $32 \pm 4 \mu\text{M}$ for DON⁹, would drive the equilibrium towards 3-*epi*-DON formation.

In conclusion, this comprehensive analysis of DepB_{Rleg} provides extensive insights into the AKR18 family. As evidenced by this structure–function study, DepB_{Rleg} presents as a versatile biocatalyst owing to its broad substrate specificity and a large active site which can accommodate a range of toxic endogenous aldehydes and ketones. The availability of the crystal structure of the enzyme should also facilitate future protein engineering work in targeting residues in the vicinity of the proposed substrate-binding site to improve the diastereoselectivity of the enzyme. While the feasibility of employing DepB in DON detoxification applications remains a contentious issue due to its NADPH dependence, this study provides a translational framework to modify its coenzyme specificity.

Materials and methods

Chemicals. 3-keto-DON, DON, and E-ascladiol were purchased from TripleBond (ON, Canada). Patulin, citrinin, 4-oxo-2-nonenal, and 4-hydroxynonenal were purchased from Cayman Chemicals (MI, USA). 3-*epi*-DON was previously purified and the identity was confirmed via LC-MS⁶. All other chemicals unless otherwise stated were from Sigma-Aldrich and Thermofisher.

Protein expression and purification. His-tagged DepB_{Rleg} and variants were recombinantly expressed in *E. coli* BL21 LOBSTR (low background strain). This engineered strain minimizes background contamination by histidine-rich *E. coli* proteins such as SlyD and ArnA during Ni-NTA chromatography⁵⁹. An overnight starter culture was used to inoculate 4L of LB media and cultures were grown at 37 °C with shaking speed at 200 RPM. Recombinant protein expression was induced with 1 mM isopropyl β -D-1-thiogalactopyranoside (IPTG) and incubated at 15 °C overnight with shaking. Cells were harvested by centrifugation and washed with 20 mM HEPES pH 8.0. The pellet was resuspended in 20 mM HEPES pH 8.0 buffer containing up to 1 mg/mL DNase I and lysed by 7–8 passages through a French press at 15,000 lb/in². Cell debris was removed through centrifugation at 4 °C and the clarified lysate filtered through a 0.45 μm filter before incubation for 1 h at 4 °C with Ni²⁺-NTA resin in buffer (50 mM sodium phosphate buffer pH 8.0, 300 mM NaCl) with binding buffer (20 mM imidazole pH 8, 150 mM NaCl). The mixture was loaded onto a gravity column and washed with the same binding buffer. His-tagged proteins were eluted with 150 mM imidazole pH 8. Buffer exchange with 20 mM HEPES pH 7.5 with 10% glycerol and 150 mM NaCl was conducted in a stirred cell equipped with a YM10 filter (Amicon). Protein concentration was determined using a Bradford Assay⁶⁰ with Bovine Serum Albumin used as a standard. The purity of the recombinant enzyme and the molecular weight of recombinant DepB_{Rleg} and coenzyme variants was estimated using Coomassie blue-stained SDS-PAGE.

Molecular weight determination. The absolute molecular weight of DepB_{Rleg} was determined using Size Exclusion Chromatography coupled with Multi-Angle Light Scattering (SEC-MALS). The column utilized for size exclusion was a P3000 single-pore GPC/SEC column (Malvern Panalytical). The system was equilibrated with the following buffer system: 20 mM HEPES, 150 mM NaCl, 0.02% NaN₃ at pH 7. The concentration of the protein samples was 0.5 mg/mL and samples were filtered through 0.2 μm filters prior to injection.

Crystallization and X-ray diffraction collection. Crystallization conditions for DepB_{Rleg} were screened using the JCSG-plus™ kit (Molecular Dimensions) and an initial hit was obtained in condition B1 (0.1 M citrate pH 4, 0.8 M ammonium sulfate). Condition B1 was optimized and a crystal was obtained in the following

optimized condition: 0.8 M ammonium sulfate, 20 mM ammonium acetate, and 0.1 M TRIS citrate. The protein was crystallized at 11 mg/mL in the presence of 400 μ M NADP⁺ via sitting drop vapor diffusion at 288 K. X-ray diffraction data were collected at the Canadian Macromolecular Crystallography Facility (CMCF-BM), processed using XDS, and scaled using XSCALE⁶¹. Crystals diffracted to 2.5 Å, and belonged to the space group *P4₂1₂*, with unit-cell parameters $a = b = 159.45$, $c = 163.9$ Å. The crystal structure of DepB_{Rleg} was solved using the automated molecular replacement pipeline, MrBUMP which generates an exhaustive list of search models. First, multiple sequence alignments are conducted between the query and homologous protein structures, second, the top hits are subjected to model preparation using a suite of CCP4 programs and finally, the models are submitted to Phaser for molecular replacement⁶². The best search model prepared from this process is the AKR from *Polaromonas* sp. JS666. AutoBuild and subsequent refinements were conducted in PHENIX⁶³ and final model building was conducted in COOT⁶⁴.

Molecular determinants of coenzyme specificity. Structural alignments were conducted via the DALI server⁶⁵. The ternary complex of the AKR6A2 member, *Rattus norvegicus* voltage-dependent K⁺ channel beta subunit (Kv β) (PDB ID: 3EAU) was superimposed on to the apo-DepB_{Rleg} structure. Structures were visualized in PyMOL (Schrödinger, Inc.) and torsion angles of residues were adjusted in the DepB_{Rleg} structure to prevent steric clash with the 2' monophosphate and the nicotinamide ring of NADP⁺. Putative residues involved in NADPH specificity were selected within a 4–5 Å distance from the 2' monophosphate attached to the adenosine ribose. Multiple sequence alignments were constructed in UGENE⁶⁶ using representative sequences from each AKR family and aligned using the MUSCLE algorithm⁶⁷. Based on this analysis, the following residues were selected as candidates for mutagenesis: Lys-217, Arg-290 and Gln-294.

Mutagenesis. Site-specific mutagenesis and mutagenic primer design were conducted as per the Single-Primer Reactions IN Parallel (SPRINP) protocol previously described⁶⁸. The wild type DepB_{Rleg} plasmid construct (pET28aDepB_{Rleg}) was used as a template with single point mutation oligonucleotide primers (Integrated DNA Technologies) and Q5 High-Fidelity DNA Polymerase (New England Biolabs). All variant constructs were confirmed by a double restriction digest (NdeI/HindIII) followed by sequence analysis conducted at (AFL) Laboratory Services Division at the University of Guelph. All primers used for mutagenesis are listed in Supplementary Table S2.

SSN construction and cluster analysis. The AKR SSN was constructed as previously described⁶⁹. The master list of AKR sequences was downloaded from UniProt using the PFAM identifier (PF00248). In total, 318,574 sequences were retrieved, and the dataset was reduced by iteratively clustering the sequences using the H-CD-HIT server⁷⁰. Sequences were then filtered based on an amino acid length cutoff between 320–350 to remove fragments and AKRs part of large multi-domain complexes. Finally, curated sequences from the AKR Database (<https://hosting.med.upenn.edu/akr/>) and the PDB were also added to the list of sequences, and any duplicates were removed by submission to CD-HIT with the sequence identity cut-off parameter set at 100%. An in-house BLAST search against this finalized database was then conducted at varying E-values and the resulting network was visualized using Cytoscape⁷¹. An optimal stringency threshold was selected to minimize the extensive fragmentation of the network.

Differential scanning fluorimetry. The thermal stability of wild-type DepB_{Rleg} and variants were assessed using SYPRO Orange while fluorescence was monitored with a StepOnePlus Real-Time PCR system (Applied Biosystems, Foster City, U.S.A.). Experiments were carried out in triplicate in 100 mM HEPES pH 7.5 with a final protein concentration of 0.3 mg/mL and 1X stock of 5000X Sypro Orange as previously described⁷² (See Supplementary Table 3).

Tryptophan quenching assays. Dissociation constants (K_d) of DepB_{Rleg} and each coenzyme was determined using a tryptophan fluorescence-quenching assay with the PTI Fluorimeter (with FelixGX software). Excitation and emission wavelengths of 295 nm and 335 nm respectively were used while slit widths were fixed at 4 nm. Titrations were performed in 20 mM HEPES pH 7.5 with 120 μ g of protein. The absorbance of only protein and buffer was measured before the assay to minimize any inner filter effects. All assays were conducted in triplicate. The change in fluorescence (ΔF) relative to the control (protein and buffer) was determined and then plotted against the concentration of each respective coenzyme. The data were fitted to the following equation⁷³ by nonlinear regression using GraphPad Prism Version 8 software to determine the K_d :

$$\Delta F = \frac{\Delta F_{\max} + [L]}{K_d + [L]}, \quad \Delta F = F_0 - F$$

F is the protein fluorescence intensity at varying concentrations of either NADPH or NADH represented by $[L]$, and F_0 is the fluorescence intensity of the protein in the absence of coenzyme.

In vitro enzyme assays. For substrate specificity experiments, reactions were carried out in 1 mL reaction volumes consisting of 100 mM HEPES pH 7.5 buffer with the NADPH concentration fixed at 1 mM. The kinetic parameters for NADPH and NADH were determined with DL-glyceraldehyde concentration fixed at 10 mM. Substrate utilization was monitored by the decrease in absorbance of NADPH or NADH at 380 nm ($\epsilon = 1132 \text{ M}^{-1} \text{ cm}^{-1}$) using the Varian Cary 100 spectrophotometer at 298 K. The rates of NADPH oxidation in the absence of enzyme were subtracted from the measured rates. NADPH was maintained under saturat-

ing conditions, for this reason, reactions were monitored at 380 nm due to the high absorbance of NADPH at 340 nm. Reactions were conducted in triplicate and initiated upon the addition of the enzyme ranging between 6 and 787 μg . One unit of enzyme is defined as the amount of enzyme required to oxidize 1 μmol of NADPH per minute. Each assay was monitored for a time period of 10 min. Stock solutions of substrates were prepared in dimethyl sulfoxide (DMSO) and the amount of substrate added to the cuvette was adjusted to ensure that DMSO concentrations were about 10% of the reaction volume to minimize inhibition of enzyme activity (no more than 9% reduction in enzyme activity).

HPLC analysis. Samples and standards were analyzed using an HPLC system (Agilent Technology 1200 Series, Palo Alto, CA, USA) equipped with a quaternary pump, an inline degasser, and a diode array detector set at 218 nm. A Phenomenex[®] 4 μ Jupiter Proteo 90A (250 \times 4.6 mm) with a C18 guard column (Torrance, CA, USA) was used for the separation. DON, 3-keto-DON, and 3-*epi*-DON were eluted using a binary mobile phase set at a flow rate of 1.0 mL/min. The composition of the mobile phase was acetonitrile: water (10:90) for DON/3-*epi*-DON and acetonitrile:water (20:80) for 3-keto-DON. The injection volume was 10 μL .

LC-MS/MS for patulin degradation products. The LC-MS/MS analysis was conducted using a Thermo[®] Scientific Q-Exactive[™] Orbitrap mass spectrometer equipped with a Vanquish[™] Flex Binary UPLC System (Waltham, MA, USA). Kinetex F5 100A column (150 \times 4.6 mm, 2.6 μm) (Phenomenex) was used for separation. The binary mobile phase consisted of solvent A (99.9% H_2O /0.1% formic acid, and solvent B (99.9% acetonitrile/0.1% formic acid). The chromatographic elution conditions were as follows: 0–16 min—5% B; 16–17 min—5–100% B; 17–21 min—100% B; 21–22 min—100–5% B; 22–28 min—5% B. The column compartment was kept at 22 $^\circ\text{C}$; the flow rate was set at 0.3 mL/min; the injection volume was 10 μL ; UV = 276 nm. The heated electrospray ionization (HESI) source was used in positive mode for the ionization of the target compounds; DDMS (top 10) mode was used, with NCE set at 30.

Diastereoselectivity assays. DepB_{Rleg} at a final concentration of 9 $\mu\text{g}/\text{mL}$ was incubated with 170 μM of 3-keto-DON, 400 μM NADPH and 50 mM TRIS pH 8, 150 mM NaCl. The reaction was incubated overnight and quenched with acetonitrile. Tubes were vortexed and left to stand for 10 min before filtration with a 0.45 μm filter. Samples were stored at $-20\text{ }^\circ\text{C}$ until ready for HPLC analysis.

Data availability

Coordinates for the DepB_{Rleg} structure have been deposited in the Worldwide Protein Data Bank (wwPDB) with the PDB accession code: 7UTF. Data from this study can be requested from the corresponding author Stephen YK Seah.

Received: 1 May 2022; Accepted: 23 August 2022

Published online: 30 August 2022

References

- Keller, N. P. Fungal secondary metabolism: Regulation, function and drug discovery. *Nat. Rev. Microbiol.* **17**, 167–180 (2019).
- Desjardins, A. E., Hohn, T. M. & McCormick, S. P. Trichothecene biosynthesis in *Fusarium* species: Chemistry, genetics, and significance. *Microbiol. Rev.* **57**, 595–604 (1993).
- Desjardins, A. *et al.* Mycotoxins: Risks in plant, animal, and human systems. *Mycopathologia* **65**, 2 (2003).
- Pierron, A. *et al.* Microbial biotransformation of DON: Molecular basis for reduced toxicity. *Sci. Rep.* **6**, 1–13 (2016).
- Wang, W. *et al.* The ribosome-binding mode of trichothecene mycotoxins rationalizes their structure: Activity relationships. *Int. J. Mol. Sci.* **22**, 1–17 (2021).
- He, J. W. *et al.* An epimer of deoxynivalenol: Purification and structure identification of 3-*epi*-deoxynivalenol. *Food Addit. Contam. Part A Chem. Anal. Control. Expo. Risk Assess.* **32**, 1523–1530 (2015).
- He, J. W. *et al.* Toxicology of 3-*epi*-deoxynivalenol, a deoxynivalenol-transformation product by *Devosia mutans* 17-2-E-8. *Food Chem. Toxicol.* **84**, 250–259 (2015).
- Hassan, Y. I. *et al.* The enzymatic epimerization of deoxynivalenol by *Devosia mutans* proceeds through the formation of 3-keto-DON intermediate. *Sci. Rep.* **7**, 1–11 (2017).
- Carere, J., Hassan, Y. I., Lepp, D. & Zhou, T. The enzymatic detoxification of the mycotoxin deoxynivalenol: Identification of DepA from the DON epimerization pathway. *Microb. Biotechnol.* **11**, 1106–1111 (2018).
- Carere, J., Hassan, Y. I., Lepp, D. & Zhou, T. The identification of DepB: An enzyme responsible for the final detoxification step in the deoxynivalenol epimerization pathway in *Devosia mutans* 17-2-E-8. *Front. Microbiol.* **9**, 1–9 (2018).
- Hoog, S. S., Pawlowski, J. E., Alzari, P. M., Penning, T. M. & Lewis, M. Three-dimensional structure of rat liver 3 α -hydroxysteroid/dihydrodiol dehydrogenase: A member of the aldo-keto reductase superfamily. *Proc. Natl. Acad. Sci. U. S. A.* **91**, 2517–2521 (1994).
- Matsunaga, T. *et al.* Involvement of an aldo-keto reductase (AKR1C3) in redox cycling of 9,10-phenanthrenequinone leading to apoptosis in human endothelial cells. *Chem. Biol. Interact.* **181**, 52–60 (2009).
- Li, D. & Ellis, E. M. Aldo-keto reductase 7A5 (AKR7A5) attenuates oxidative stress and reactive aldehyde toxicity in V79–4 cells. *Toxicol. Vitro* **28**, 707–714 (2014).
- Guengerich, F. P. *et al.* Reduction of aflatoxin B1 dialdehyde by rat and human aldo-keto reductases. *Chem. Res. Toxicol.* **14**, 727–737 (2001).
- Laffin, B. & Petrash, J. M. Expression of the aldo-keto reductases AKR1B1 and AKR1B10 in human cancers. *Front. Pharmacol.* **3** JUN, 1–7 (2012).
- Tang, W. H., Martin, K. A. & Hwa, J. Aldose reductase, oxidative stress, and diabetic mellitus. *Front. Pharmacol.* **3**(MAY), 1–8 (2012).
- Vander Jagt, D. L., Robinson, B., Taylor, K. K. & Hunsaker, L. A. Reduction of trioses by NADPH-dependent aldo-keto reductases. Aldose reductase, methylglyoxal, and diabetic complications. *J. Biol. Chem.* **267**, 4364–4369 (1992).
- Hyndman, D., Bauman, D. R., Heredia, V. V. & Penning, T. M. The aldo-keto reductase superfamily homepage. *Chem. Biol. Interact.* **143–144**, 621–631 (2003).

19. Jez, J. M., Flynn, T. G. & Penning, T. M. A nomenclature system for the aldo-keto reductase superfamily. *Adv. Exp. Med. Biol.* **414**, 579–589 (1997).
20. Gerlt, J. A. *et al.* Enzyme function initiative-enzyme similarity tool (EFI-EST): A web tool for generating protein sequence similarity networks. *Biochim. Biophys. Acta Proteins Proteom.* **1854**, 1019–1037 (2015).
21. Jez, J. M. & Penning, T. M. The aldo-keto reductase (AKR) superfamily: An update. *Chem. Biol. Interact.* **130–132**, 499–525 (2001).
22. He, W. J. *et al.* An aldo-keto reductase is responsible for Fusarium toxin-degrading activity in a soil *Sphingomonas* strain. *Sci. Rep.* **7**, 1–13 (2017).
23. Bate, N., Butler, A. R., Smith, I. P. & Cundliffe, E. The mycarose-biosynthetic genes of *Streptomyces fradiae*, producer of tylosin. *Microbiology* **146**, 139–146 (2000).
24. Summers, R. G. *et al.* Sequencing and mutagenesis of genes from the erythromycin biosynthetic gene cluster of *Saccharopolyspora erythraea* that are involved in L-mycarose and D-desosamine production. *Microbiology* **143**, 3251–3262 (1997).
25. Ikeda, H., Nonomiya, T., Usami, M., Ohta, T. & Omura, S. Organization of the biosynthetic gene cluster for the polyketide anthelmintic macrolide avermectin in *Streptomyces avermitilis*. *Proc. Natl. Acad. Sci. U. S. A.* **96**, 9509–9514 (1999).
26. Wonisch, W., Schaur, R. J., Bilinski, T. & Esterbauer, H. Assessment of growth inhibition by aldehydic lipid peroxidation products and related aldehydes by *Saccharomyces cerevisiae*. *Cell Biochem. Funct.* **13**, 91–98 (1995).
27. Semchysyn, H. M. Reactive carbonyl species in vivo: Generation and dual biological effects. *Sci. World J.* **2014**, 27–31 (2014).
28. Ciegler, A., Vesonder, R. F. & Jackson, L. K. Production and biological activity of patulin and citrinin from *Penicillium expansum*. *Appl. Environ. Microbiol.* **33**, 1004–1006 (1977).
29. Tannous, J. *et al.* Patulin transformation products and last intermediates in its biosynthetic pathway, E- and Z-ascladiol, are not toxic to human cells. *Arch. Toxicol.* **91**, 2455–2467 (2017).
30. Tannous, J. *et al.* Sequencing, physical organization and kinetic expression of the patulin biosynthetic gene cluster from *Penicillium expansum*. *Int. J. Food Microbiol.* **189**, 51–60 (2014).
31. Ianiri, G. *et al.* Searching for genes responsible for patulin degradation in a biocontrol yeast provides insight into the basis for resistance to this mycotoxin. *Appl. Environ. Microbiol.* **79**, 3101–3115 (2013).
32. Kadumuri, R. V. & Vadrevu, R. Diversity in $\alpha\beta$ and $\beta\alpha$ Loop connections in TIM barrel proteins: Implications for stability and design of the fold. *Interdiscip. Sci. Comput. Life Sci.* **10**, 805–812 (2018).
33. Borhani, D. W., Harter, T. M. & Petrash, J. M. The crystal structure of the aldose reductase-NADPH binary complex. *J. Biol. Chem.* **267**, 24841–24847 (1992).
34. Krissinel, E. & Henrick, K. Detection of protein assemblies in crystals. In 163–174. https://doi.org/10.1007/11560500_15 (2005).
35. Obmolova, G. *et al.* Crystal structure of the *Escherichia coli* Tas protein, an NADP(H)-dependent aldo-keto reductase. *Proteins Struct. Funct. Genet.* **53**, 323–325 (2003).
36. Laphorn, A. J., Zhu, X. & Ellis, E. M. The diversity of microbial aldo/keto reductases from *Escherichia coli* K12. *Chem. Biol. Interact.* **202**, 168–177 (2013).
37. Wheeler, R. *et al.* Discovery of a cryptic intermediate in late steps of Mithramycin biosynthesis. *Angew. Chemie Int. Ed.* **59**, 826–832 (2020).
38. Sanli, G., Dudley, J. I. & Blaber, M. Structural biology of the aldo-keto reductase. *Cell Biochem. Biophys.* **38**, 79–101 (2003).
39. Kwon, S. G. *et al.* Important role of the C-terminal region of pig aldo-keto reductase family 1 member C1 in the NADPH-dependent reduction of steroid hormones. *Indian J. Biochem. Biophys.* **50**, 237–241 (2013).
40. Penning, T. M. The aldo-keto reductases (AKRs): Overview. *Chem. Biol. Interact.* **234**, 236–246 (2015).
41. Ishikura, S. *et al.* Characterization of two isoforms of mouse 3(17) α -hydroxysteroid dehydrogenases of the aldo-keto reductase family. *Biol. Pharm. Bull.* **27**, 1939–1945 (2004).
42. Zhang, Y., Dufort, I. & Rheault, P. Characterization of a human 20-hydroxysteroid dehydrogenase. *J. Mol. Endocrinol.* **25**, 221–228 (2000).
43. Handumrongkul, C., Ma, D.-P. & Silva, J. L. Cloning and expression of *Candida guilliermondii* xylose reductase gene (xyl1) in *Pichia pastoris*. *Appl. Microbiol. Biotechnol.* **49**, 399–404 (1998).
44. Kavanagh, K. L., Klimacek, M., Nidetzky, B. & Wilson, D. K. Structure of xylose reductase bound to NAD⁺ and the basis for single and dual co-substrate specificity in family 2 aldo-keto reductases. *Biochem. J.* **373**, 319–326 (2003).
45. Amore, R., Kötter, P., Küster, C., Ciriacy, M. & Hollenberg, C. P. Cloning and expression in *Saccharomyces cerevisiae* of the NAD(P) H-dependent xylose reductase-encoding gene (XYL1) from the xylose-assimilating yeast *Pichia stipitis*. *Gene* **109**, 89–97 (1991).
46. Liu, S. Q., Jin, H., Zacarias, A., Srivastava, S. & Bhatnagar, A. Binding of pyridine nucleotide coenzymes to the β -subunit of the voltage-sensitive K⁺ channel. *J. Biol. Chem.* **276**, 11812–11820 (2001).
47. Ellis, E. M. & Hayes, J. D. Substrate specificity of an aflatoxin-metabolizing aldehyde reductase. *Biochem. J.* **312**, 535–541 (1995).
48. Yokochi, N., Yoshikane, Y., Trongpanich, Y., Ohnishi, K. & Yagi, T. Molecular cloning, expression, and properties of an unusual aldo-keto reductase family enzyme, pyridoxal 4-dehydrogenase, that catalyzes irreversible oxidation of pyridoxal. *J. Biol. Chem.* **279**, 37377–37384 (2004).
49. Jez, J. M., Bennett, M. J., Schlegel, B. P., Lewis, M. & Penning, T. M. Comparative anatomy of the aldo-keto reductase superfamily. *Biochem. J.* **326**, 625–636 (1997).
50. Tipparaju, S. M., Barski, O. A., Srivastava, S. & Bhatnagar, A. Catalytic mechanism and substrate specificity of the β -subunit of the voltage-gated potassium channel. *Biochemistry* **47**, 8840–8854 (2008).
51. Ma, H., Ratnam, K. & Penning, T. M. Mutation of nicotinamide pocket residues in rat liver 3 α -hydroxysteroid dehydrogenase reveals different modes of cofactor binding. *Biochemistry* **39**, 102–109 (2000).
52. Paidimuddala, B., Mohapatra, S. B., Gummadi, S. N. & Manoj, N. Crystal structure of yeast xylose reductase in complex with a novel NADP-DTT adduct provides insights into substrate recognition and catalysis. *FEBS J.* **285**, 4445–4464 (2018).
53. Wang, Z. *et al.* Semi-rational engineering of a thermostable aldo-keto reductase from *Thermotoga maritima* for synthesis of enantiopure ethyl-2-hydroxy-4-phenylbutyrate (EHPB). *Sci. Rep.* **7**, 1–11 (2017).
54. Grant, A. W., Steel, G., Waugh, H. & Ellis, E. M. A novel aldo-keto reductase from *Escherichia coli* can increase resistance to methylglyoxal toxicity. *FEMS Microbiol. Lett.* **218**, 93–99 (2003).
55. Streeter, C. C., Lin, Q. & Firestone, S. M. Isatins inhibit N5 -CAIR synthetase by a substrate depletion mechanism. *Biochemistry* **58**, 2260–2268 (2019).
56. Xing, M., Chen, Y., Li, B. & Tian, S. Characterization of a short-chain dehydrogenase/reductase and its function in patulin biodegradation in apple juice. *Food Chem.* **348**, 129046 (2021).
57. Chan, E. T. S., Zhu, Y., Li, X.-Z., Zhou, T. & Seah, S. Y. K. Characterization of two dehydrogenases from *Gluconobacter oxydans* involved in the transformation of patulin to ascladiol. *Toxins (Basel)*, **14**, 423 (2022).
58. Baker, P. J., Britton, K. L., Rice, D. W., Rob, A. & Stillman, T. J. Structural consequences of sequence patterns in the fingerprint region of the nucleotide binding fold. Implications for nucleotide specificity. *J. Mol. Biol.* **228**, 662–671 (1992).
59. Andersen, K. R., Leska, N. C., Schwartz, T. U. & Optimized, E. coli expression strain LOBSTR eliminates common contaminants from His-tag purification. *Proteins* **81**, 1857–1861 (2013).
60. Bradford, M. M. A rapid and sensitive method for the quantitation of microgram quantities of protein utilizing the principle of protein-dye binding. *Anal. Biochem.* **72**, 248–254 (1976).
61. Kabsch, W. XDS. *Acta Crystallogr. Sect. D Biol. Crystallogr.* **66**, 125–132 (2010).

62. Keegan, R. M. & Winn, M. D. MrBUMP: An automated pipeline for molecular replacement. *Acta Crystallogr. Sect. D Biol. Crystallogr.* **64**, 119–124 (2007).
63. Liebschner, D. *et al.* Macromolecular structure determination using X-rays, neutrons and electrons: Recent developments in Phenix. *Acta Crystallogr. Sect. D Struct. Biol.* **75**, 861–877 (2019).
64. Emsley, P., Lohkamp, B., Scott, W. G. & Cowtan, K. Features and development of Coot. *Acta Crystallogr. Sect. D Biol. Crystallogr.* **66**, 486–501 (2010).
65. Holm, L., Käriäinen, S., Wilton, C. & Plewczynski, D. Using Dali for structural comparison of proteins. In *Current Protocols in Bioinformatics* (eds Baxevanis, A. D. *et al.*) (Wiley, 2006). <https://doi.org/10.1002/0471250953.bi0505s14>.
66. Okonechnikov, K. *et al.* Unipro UGENE: A unified bioinformatics toolkit. *Bioinformatics* **28**, 1166–1167 (2012).
67. Edgar, R. C. MUSCLE: A multiple sequence alignment method with reduced time and space complexity. *BMC Bioinform.* **5**, 1–19 (2004).
68. Edelheit, O., Hanukoglu, A. & Hanukoglu, I. Simple and efficient site-directed mutagenesis using two single-primer reactions in parallel to generate mutants for protein structure-function studies. *BMC Biotechnol.* **9**, 1–8 (2009).
69. Copp, J. N., Akiva, E., Babbitt, P. C. & Tokuriki, N. Revealing unexplored sequence-function space using sequence similarity networks. *Biochemistry* **57**, 4651–4662 (2018).
70. Li, W., Jaroszewski, L. & Godzik, A. Clustering of highly homologous sequences to reduce the size of large protein databases. *Bioinformatics* **17**, 282–283 (2001).
71. Shannon, P. *et al.* Cytoscape: A software environment for integrated models. *Genome Res.* **13**, 426 (1971).
72. Turner, M., Heney, K. A. & Rod Merrill, A. The N-terminus of *Paenibacillus* larvae C3larvinA modulates catalytic efficiency. *Biosci. Rep.* **41**, 1–16 (2021).
73. Wang, W. & Seah, S. Y. K. Purification and biochemical characterization of a pyruvate-specific class II aldolase, HpaI. *Biochemistry* **44**, 9447–9455 (2005).

Acknowledgements

The authors would like to thank Xiu-Zhen Li and Lili Mats (Agriculture and AgriFood Canada) as well as Dr. Rod Merrill and Chau Tran (University of Guelph). The financial support from Agriculture and Agri-Food Canada and Grain Farmers of Ontario through the Industry-led Research and Development Project (J-002433) is acknowledged and much appreciated.

Author contributions

N.A. and S.Y.K.S. designed the study. N.A. and S.Y.K.S. wrote the manuscript and prepared the figures. N.A., K.S., Y.Z. J.C. and N.E. conducted the reported experiments. N.A. and M.S.K. performed molecular modeling. N.A. and S.Y.K.S. interpreted the results. N.A. and S.Y.K.S. integrated all research. J.C. reviewed and edited the manuscript. T.Z. obtained research funding and is involved in the conception and supervision of the research project. All authors discussed the results and commented on the manuscript.

Competing interests

The authors declare no competing interests.

Additional information

Supplementary Information The online version contains supplementary material available at <https://doi.org/10.1038/s41598-022-19040-8>.

Correspondence and requests for materials should be addressed to S.Y.K.S.

Reprints and permissions information is available at www.nature.com/reprints.

Publisher's note Springer Nature remains neutral with regard to jurisdictional claims in published maps and institutional affiliations.



Open Access This article is licensed under a Creative Commons Attribution 4.0 International License, which permits use, sharing, adaptation, distribution and reproduction in any medium or format, as long as you give appropriate credit to the original author(s) and the source, provide a link to the Creative Commons licence, and indicate if changes were made. The images or other third party material in this article are included in the article's Creative Commons licence, unless indicated otherwise in a credit line to the material. If material is not included in the article's Creative Commons licence and your intended use is not permitted by statutory regulation or exceeds the permitted use, you will need to obtain permission directly from the copyright holder. To view a copy of this licence, visit <http://creativecommons.org/licenses/by/4.0/>.

© The Author(s) 2022